Acta Oceanol. Sin., 2024, Vol. 43, No. 1, P. 48–58
https://doi.org/10.1007/s13131-023-2278-3
http://www.aosocean.com
E-mail: ocean2@hyxb.org.cn

Seasonal variation of mesoscale eddy intensity in the global ocean

Yongcan Zu[1, 2, 3], Yue Fang[1, 2, 3*], Shuangwen Sun[1, 2, 3], Libao Gao[1, 2, 3], Yang Yang[1, 2, 3], Guijun Guo[1, 2, 3]

[1] First Institute of Oceanography/Key Laboratory of Marine Science and Numerical Modeling, Ministry of Natural Resources, Qingdao 266061, China

[2] Laboratory for Regional Oceanography and Numerical Modeling, Laoshan Laboratory, Qingdao 266237, China

[3] Shandong Key Laboratory of Marine Science and Numerical Modeling, Qingdao 266061, China

Received 3 June 2023; accepted 9 November 2023

Abstract

Mesoscale eddies are a prominent oceanic phenomenon that plays an important role in oceanic mass transport and energy conversion. Characterizing by rotational speed, the eddy intensity is one of the most fundamental properties of an eddy. However, the seasonal spatiotemporal variation in eddy intensity has not been examined from a global ocean perspective. In this study, we unveil the seasonal spatiotemporal characteristics of eddy intensity in the global ocean by using the latest satellite-altimetry-derived eddy trajectory data set. The results suggest that the eddy intensity has a distinct seasonal variation, reaching a peak in spring while attaining a minimum in autumn in the Northern Hemisphere and the opposite in the Southern Hemisphere. The seasonal variation of eddy intensity is more intense in the tropical-subtropical transition zones within latitudinal bands between 15° and 30° in the western Pacific Ocean, the northwestern Atlantic Ocean, and the eastern Indian Ocean because baroclinic instability in these areas changes sharply. Further analysis found that the seasonal variation of baroclinic instability precedes the eddy intensity by a phase of 2–3 months due to the initial perturbations needing time to grow into mesoscale eddies.

Key words: seasonal variation, mesoscale eddy, intensity, baroclinic instability, global ocean

Citation: Zu Yongcan, Fang Yue, Sun Shuangwen, Gao Libao, Yang Yang, Guo Guijun. 2024. Seasonal variation of mesoscale eddy intensity in the global ocean. Acta Oceanologica Sinica, 43(1): 48–58, doi: 10.1007/s13131-023-2278-3

1 Introduction

Oceanic mesoscale eddies are coherent rotating vortices of water with radius scales in the order of 10–100 km and lifetimes of several days to months that are nearly omnipresent mesoscale phenomena in the global ocean (Chelton et al., 2011b; Faghmous et al., 2015). Most mesoscale eddies propagate westward, and their propagation distances can reach thousands of kilometers (Chelton et al., 2011b). Mesoscale eddies can induce strong thermohaline anomalies and vertically extend up to a depth of thousands of meters (Chu et al., 2014; Sun et al., 2017; Zu et al., 2019). These characteristics of mesoscale eddies make them play a significant role in transporting oceanic mass (Zhang et al., 2014), heat and salt (Chen et al., 2012; Dong et al., 2014; Yang et al., 2015), pollutants (Chen et al., 2021), nutrient and marine phytoplankton (Chelton et al., 2011a; Frenger et al., 2018; Zhou et al., 2023), and regulating local atmospheric systems (Frenger et al., 2013). Influenced by the seasonality of the upper ocean, eddy properties not only have seasonal variation (Shum et al., 1990; Andersson et al., 2011), but some tracers (e.g., chlorophyll) trapped by eddies also change with seasonality (Gaube et al., 2014). Compared with the eddy trapping component, the eddy stirring component is distinctly larger in most areas (Sun et al., 2019). As one of the most fundamental properties of an eddy, the eddy intensity has a significant effect both on the eddy trapping component and the eddy stirring component of eddy-induced material transport (Gaube et al., 2014; Zu et al., 2019). Therefore, clarifying the seasonal feature of eddy intensity is essential to evaluate the impact of eddies on air-sea interactions and marine ecosystems.

Using satellite altimeter products and eddy detection algorithms, previous studies have analyzed eddy properties (such as size, lifetime, number, amplitude) in the regional and global oceans. On a regional scale, many studies have focused on the seasonal variation of eddy generation numbers in different areas of the global ocean, including the Pacific Ocean (Chaigneau et al., 2009; Kurczyn et al., 2012; Liu et al., 2012), the Atlantic Ocean (Chaigneau et al., 2008, 2009; Schütte et al., 2016), the Indian Ocean (Halo et al., 2014), and the Southern Ocean (Frenger et al., 2015). These studies show that the seasonal characteristics of generated eddies are diverse within corresponding regional oceans, which indicates that the size and location of the study regions greatly disturb the results of statistical analysis for eddy

Foundation item: The National Key R&D Program of China under contract No. 2022YFC2807604; the Basic Scientific Fund for National Public Research Institutes of China under contract Nos 2022S02, 2022Q03 and 2018S02; the Marine S&T Fund of Shandong Province for Pilot National Laboratory for Marine Science and Technology (Qingdao) under contract No. 2018SDKJ0105-3; the National Natural Science Foundation of China under contract Nos 41876030, 41976021, 41876231, 4190060432 and 41706220; the program Impact and Response of Antarctic Seas to Climate Change under contract No. IRASCC 01-01-01A; the Taishan Scholars Project Fund under contract No. ts20190963.

*Corresponding author, E-mail: yfang@fio.org.cn

properties. Aguedjou et al. (2019) also pointed out that eddy amplitude has a strong seasonal cycle in the North Brazil Current retroflection, while it does not show significant variability in the North Equatorial Countercurrent area because of the different mechanisms of eddy generation in these two adjacent regions. In the Leeuwin Current system, more and stronger eddies tend to be generated in austral winter, while in the South Indian Countercurrent system, eddy properties generally reach their peaks in austral spring (Zhang et al., 2020). Zu et al. (2022) reported that the eddy amplitude in an area to the southwest coast of Java Island has prominent seasonality—eddies in this area are relatively weak during the first half of the year but tend to enhance in August and peak in October. They deduced that the seasonality of eddy amplitude is due to eddy development under the conditions of seasonal energy supply mainly from baroclinic instability. In some smaller regions, the seasonal variations of eddy amplitude are more complex. For instance, in the Sulu Sea, there are more cyclonic eddies with a larger amplitude during boreal winter, while there are more anticyclonic eddies with a larger amplitude during boreal summer (He et al., 2017). In offshore regions, the mechanisms responsible for eddy generation may be multiple and more complex, e.g., the interaction of large-scale currents with bottom topography, coastline geometry or islands, local baroclinic instability, and instability of coastal currents (Chaigneau et al., 2009; He et al., 2017). On a global scale, Martínez-Moreno et al. (2022) pointed out that a strong seasonal cycle is observed in the spatially coherent eddy field based on hemispherical averages, in which the eddy amplitude peaking in September for the Northern Hemisphere and January in the Southern Hemisphere. They related the seasonal variation of eddies to the wind forcing at time lags of 3–6 months and further highlighted that the inverse energy cascade is important for the observed seasonal cycle of coherent eddy properties. However, the spatial pattern of seasonal variation is not clarified in their work. From the above findings, it can be inferred that the seasonal spatiotemporal variations in eddies may be non-uniform in the global oceans. Therefore, it is necessary to simultaneously examine the spatial pattern and temporal pattern of seasonal variation in eddies.

There are multiple variables representing the intensity of mesoscale eddies, such as eddy amplitude (the absolute difference between the average sea surface height (SSH) at the eddy boundary and the extreme value of SSH in the eddy interior (Chelton et al., 2011b), eddy rotational speed and eddy kinetic energy (EKE). Generally, eddy amplitude dominates the rotational speed of the eddy. As the rotational speed increases, the eddy nonlinearity is easier to get stronger. Here, the eddy nonlinearity parameter refers to the ratio (u/c) between the maximum rotational speed of eddies (u) and their propagation speed (c) (Chelton et al., 2011b). A u/c >1 implies that the eddies are nonlinear and thus can trap materials in their core (Chelton et al., 2011b; Kurian et al., 2011). Figure 1 displays the climatological field of u and propagation speeds c of eddies in every 2°×2° grid, which shows that most eddies are nonlinear (u/c >1). No matter eddy rotational speed or eddy amplitude, they can be tracked in the eddy lifetime and the energy represent by them is coherent, while the EKE is discrete. Meanwhile, considering the direct effect of rotational speed on the nonlinearity of an eddy, we select rotational speed, a more intuitive term "intensity", to represent eddy intensity in this study. Although eddy intensity is crucial to evaluating the transport of substances induced by eddies, its seasonal spatiotemporal characteristics on a global scale are still poorly understood. This study will analyze the spatiotemporal characteristics of eddy intensity at a seasonal scale from a global ocean perspective. The paper is organized as follows. Section 2 introduces the tracked eddy data set and relevant oceanic data. The results of seasonal variations in eddy intensity are presented in Section 3 and its main mechanism is discussed in Section 4. The paper is concluded with a summary in Section 5.

2 Data and methods

2.1 *Data*

The delayed time mesoscale eddy trajectory atlas data set 3.2 (META 3.2) is distributed by Archiving, Validation, and Interpretation of Satellite Oceanographic (AVISO). The META 3.2 based

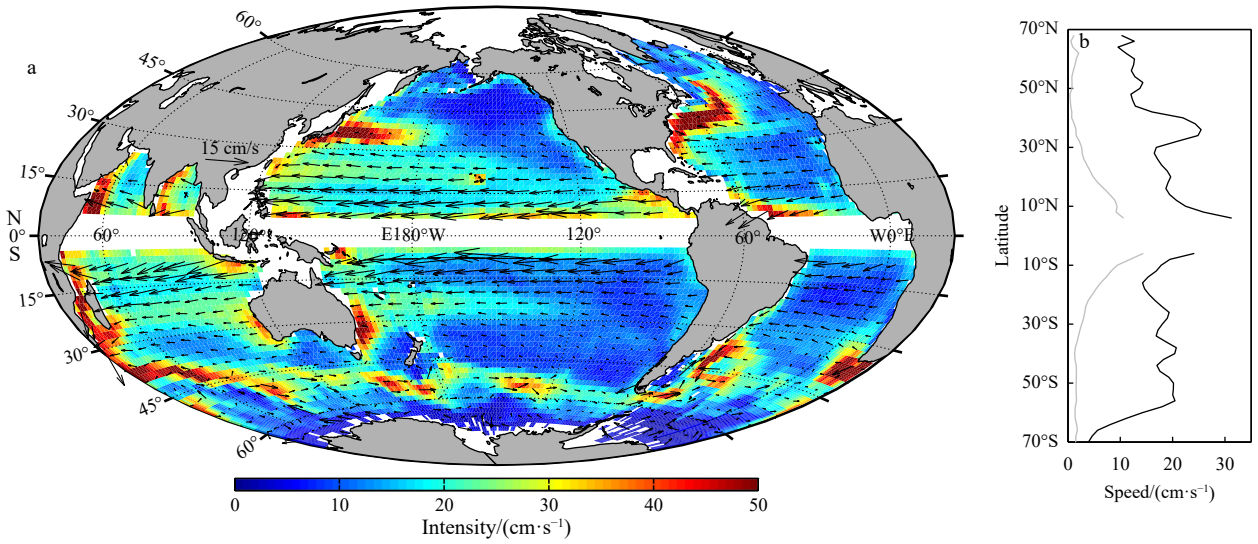

Fig. 1. Climatological field of intensity (cm/s, color) of mesoscale eddies overlapped with their propagation speeds (cm/s, arrow) (a); the climatological field of eddy intensity was averaged from the rotational speeds of eddies in every 2° × 2° grid from 1993 to 2021; the propagation speeds were calculated over the eddies' trajectory and projected into the corresponding 2° × 2° grid where the eddies formed. The zonal mean of rotational speeds (black curves) and propagation speeds (gray curves) (b).

on the all-sat merged absolute dynamic topography (ADT) fields is the latest version of the data set, which is generated and quality-controlled following the methodology developed by Mason et al. (2014) and further described in Pegliasco et al. (2022). The data set contains the positions of tracked eddies (eddy centers) as well as their properties (radius, amplitude, and rotational speed). The latter is identical to the "eddy intensity" analyzed in this study. The eddy data set spans the period from January 1993 to February 2022, covering the global ocean between 82.5°S to 82.5°N. In this study, the eddies shorter than 4 weeks and with amplitudes smaller than 1 cm are removed to exclude noise signals. The rotational speed is defined as the maximum of the average geostrophic speeds around all of the closed SSH contours inside the eddy (Chelton et al., 2011b). Besides, the daily all-satellite merged absolute geostrophic current with horizontal resolution (1/4)° × (1/4)° published by Copernicus Marine Service is also utilized.

The global ocean potential temperature and salinity (T-S) profiles are from the EN4.2.2 version of the Met Office Hadley Centre, mainly merging WOD09 and Argo float profiling data. Based on observational T-S profiles, the EN4.2.2 objective analysis monthly data set describes the ocean hydrographic conditions on a 1° spatial grid, with a vertical resolution of approximately 10–11 m from the surface to 110 m, and continues to 5 350 m with decreasing vertical resolution (Good et al., 2013).

2.2 *Methods*

First, we divide the global ocean into 2° × 2° regular grids and then count all instantaneous eddies within the corresponding grids every month. The instantaneous eddies refer to the eddies detected from the ADT snapshot for a certain moment. The monthly eddy intensity data can be obtained by calculating the mean values of the rotational speeds of all instantaneous eddies over every grid in the calendar month from January 1993 to December 2021. To more efficiently ascertain the temporal and spatial variations in eddy intensity globally, we applied an empirical orthogonal function (EOF) analysis approach to eddy intensity anomalies. The anomalies were computed by removing the climatology value which was averaged from the whole time series for each grid. To lessen the spatial discretization in grid points, spatial smoothing with 3 grid lengths was applied in the eddy intensity fields before operating the EOF. This method can effectively eliminate discrete noise signals and extract spatial change trends. The smoothing method is also necessary when considering the very low explained variance of the EOF for the raw data (figure not shown). The spatial pattern and time pattern are not sensitive to a changing grid length. Moreover, to filter out the interference of intraseasonal signals and interannual and interdecadal variations, a 3–24 months bandpass filter was also applied to the eddy intensity fields. In this study, we define spring as April to June (AMJ) and autumn as October to December (OND) in the Northern Hemisphere and vice versa in the Southern Hemisphere.

We use the Eady growth rate (EGR) to indicate baroclinic instability in the ocean (Eady, 1949; Smith, 2007), which is quantified as

$$\mathrm{EGR} = f\sqrt{\frac{1}{H}\int_{-H}^{0}\frac{\mathrm{d}z}{R_i(z)}}, \tag{1}$$

$$R_i = \frac{N^2}{|\partial U/\partial z|^2}, \tag{2}$$

where f is the Coriolis parameter, N is the buoyancy frequency (or Brunt-Väisälä frequency) calculated by using the Thermodynamic Equation of SeaWater 2010 (TEOS-10), R_i is the Richardson number and H is the water depth. $\partial U/\partial z$ is the vertical shear of the horizontal velocity, using the thermal wind balance from

$$\left|\frac{\partial U}{\partial z}\right| = \frac{g}{\rho_0 f}\sqrt{\left(\frac{\partial \rho}{\partial x}\right)^2 + \left(\frac{\partial \rho}{\partial y}\right)^2}, \tag{3}$$

where ρ is the density of seawater, ρ_0 is the reference density of seawater, and g is the gravitational acceleration. In the open oceans, the upper 200 m is the depth where remarkable seasonal variations in the ocean are concentrated (Zhai et al., 2008; Qiu and Chen, 2013). Therefore, we will focus on the depth-averaged values of EGR in the upper 200 m.

The barotropic conversion rate (BTR) is used to analyze the barotropic instability, which is defined as (Böning and Budich, 1992; Zhang et al., 2016)

$$\mathrm{BTR} = -\left(\overline{u'u'}\frac{\partial \overline{u}}{\partial x} + \overline{u'v'}\left(\frac{\partial \overline{v}}{\partial x} + \frac{\partial \overline{u}}{\partial y}\right) + \overline{v'v'}\frac{\partial \overline{v}}{\partial y}\right). \tag{4}$$

BTR is the conversion rate between mean kinetic energy (MKE) and EKE. Positive BTR implies part of the MKE of the mean flow is transferred to the EKE due to the barotropic instability. We use the absolute geostrophic velocity published by Copernicus Marine Service to represent currents in the upper layers. The transient components of velocity and density (e.g., u') are defined as variability of periods shorter than 120 d, and the residual low-frequency variations with periods larger than 120 d (e.g., $\bar{u}$) are treated as the basic state.

When conducting linear Pearson's correlation analysis of two-time series (x_1 and x_2), the effective degrees of freedom (DOF) are estimated following Bretherton et al. (1999):

$$\mathrm{DOF} = N_s\frac{1 - r_1 r_2}{1 + r_1 r_2}, \tag{5}$$

where N_s is the sample number, r_1 and r_2 are the autocorrelation coefficients of x_1 and x_2 at lag one. DOF is the number of ways or dimensions that an independent value can move without violating constraints. All data are detrended before correlation coefficients are calculated.

3 Results

3.1 *Seasonal characteristics of mesoscale eddy intensity*

To compare with the spatial patterns of seasonal variation, the climatological distributions of eddy intensity are first examined, which vary greatly across the globe (Fig. 1a). The regions with high values are primarily distributed in the strong current areas, such as the areas in the Kuroshio extension, the Gulf Stream, the Agulhas Stream, and the Somali Stream, which is consistent with the pattern of surface EKE in the work of Martínez-Moreno et al. (2022). In the subtropical regions, the zonal distribution of eddy intensity is different. At low latitudes, however, eddy intensity is also relatively strong, which is different from the distribution of eddy amplitude (Fig. S1). This may be due to the common effect of the small Coriolis force and the

strong equatorial currents in the equatorial regions.

To extract the seasonal spatiotemporal characteristics, the EOF method is applied to the monthly anomaly of eddy intensity. The spatial and temporal patterns of the first EOF mode (EOF1) of eddy intensity anomaly are displayed in Figs 2a and b, respectively. One can see that the eddy intensity shows a distinct seasonal variation (Fig. 2b). It reaches a peak in boreal spring while attaining a minimum in boreal autumn, which can be intuitively revealed by the mean annual cycles of the time pattern in Fig. 2c. Spatially, the conspicuous areas are primarily located in the tropical-subtropical transition zones within latitudinal bands between 15° and 30° in the main open oceans, except for 20° to 35° in the southern Atlantic Ocean (Fig. 2a), which is different from the regions of strong climatological eddy intensity displayed by Fig. 1a. An important feature is that the eddy intensity shows the most intense seasonal variations in the tropical-subtropical transition zones of the western Pacific Ocean, the northwestern Atlantic Ocean, and the eastern Indian Ocean, which are indicated with thick solid rectangular boxes in Fig. 2a.

It is also noted that the spatial pattern in EOF1 is nonhomogenous in zonal distributions, which is in accord with those of climatological eddy intensity. In some regions of a half hemisphere, the amplitudes of seasonal variations are opposite or very slight. To compare with the spatial differences of seasonal variations, we selected four regions with opposite or slight seasonality (shown by the thin dotted rectangular boxes in Fig. 2a) and calculated their regional mean values of eddy intensity (Fig. S2). Their seasonal variations are consistent with the change of magnitude in the corresponding region in the spatial pattern in Fig. 2a. For instance, the eddies with strong intensity in the western Arabian

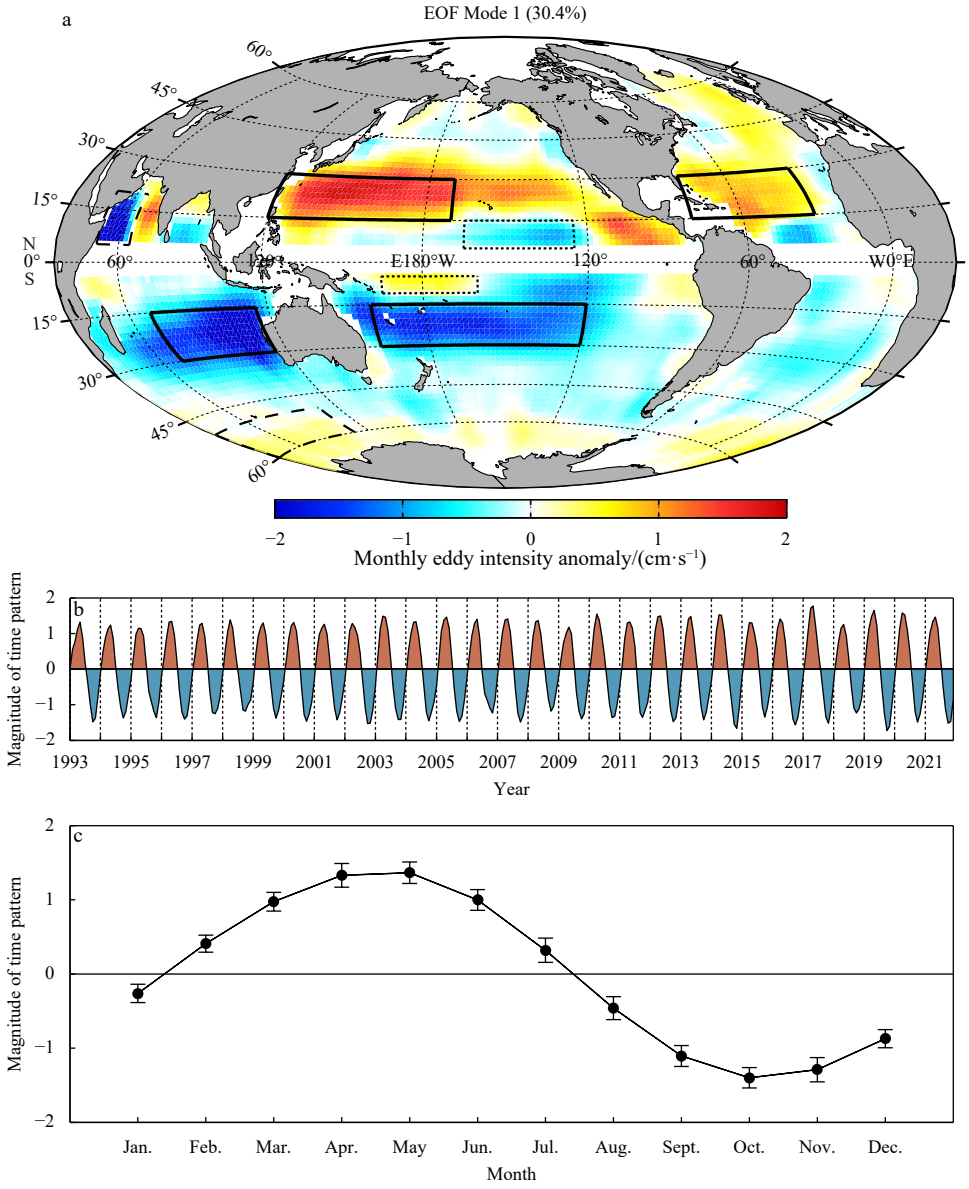

Fig. 2. First EOF mode of the monthly eddy intensity (cm/s) anomaly over the global ocean from January 1993 to December 2021: spatial pattern (a) and time pattern (b). The mode explains 30.4% of the eddy intensity variance. c. Times series of the monthly mean of the EOF1 time pattern. The error bars show the standard deviation (SD) of the eddy intensity anomalies in the corresponding month. Selected four regions with strong seasonality are indicated with thick solid rectangular boxes, and the other four regions with opposite or slight seasonality are indicated with thin dotted rectangular boxes in a.

Sea have a remarkable seasonal variation, reaching a peak in the latter half of the year (Fig. S2a). In this region, the positive increment can also be inferred from the large amplitude with a negative signal in the spatial pattern (Fig. 2a) multiplied by negative values in the time pattern in the latter half of the year (Fig. 2c). From the spatial pattern, it can be seen that seasonal spatial variations in eddies are non-uniform in the one-half hemisphere. Therefore, for the regions where eddies change strongly in opposite directions, their seasonal characteristics derived from regional averages are varied.

The spatial pattern of EOF1 is consistent with the maximum difference distribution (Fig. S3) of eddy intensity between spring and autumn, verifying the results of the EOF method for eddy intensity anomaly representing its seasonal spatiotemporal variations. Multiplying the spatial pattern and temporal pattern of EOF1 can obtain the monthly change in eddy intensity. This monthly change is smaller than the corresponding values calculated from raw data due to the smooth and filter methods applied in Fig. 2. From the raw data (Fig. S1), we can conclude that the regionally averaged eddy intensity in every spring is approximately 4.22 cm/s stronger than that in every autumn in the latitudinal bands between 15° and 30° in the northwestern Pacific Ocean (120°E–170°W). In the same latitudinal band of the western Indian Ocean (70°E–115°E), this quantity is approximately –4.59 cm/s. The maximum intensity in the seasonal cycle is approximately 1.3 times larger than the minimum counterpart in these two regions. The seasonal difference in eddy intensity represents the change in the energy source for eddy generation and development (through energy transfer) in the background.

Considering the effect of eddy polarity on the seasonality, we have calculated the climatological intensity of anticyclonic eddies (AEs) and cyclonic eddies (CEs), and their seasonal differences (Fig. 3). First of all, their spatial patterns of the climatological field are basically the same in the global scale (Figs 3a and b). In some regional areas, such as the Southeast of the North Pacific Ocean, the climatological intensity of AEs is stronger than that of CEs. There are also areas where CEs are greater than AEs, such as the Bay of Bengal and the western Arabian Sea. For the seasonal variations of AEs and CEs, it can be seen that the spatial patterns of both are also basically the same on the global scale (Figs 3c and d), especially in the areas that this study focuses on (boxes in Fig. 2a). Differences exist in some regions, such as the Southeast of North Pacific Ocean. Although there are some differences in some regional areas, it does not affect the main conclusion of this section.

3.2 *Mechanism of seasonality in mesoscale eddy intensity*

In the open oceans, eddy generation is mainly caused by baroclinic instability, which further affects eddy development (Robinson and McWilliams, 1974; Stammer, 1998; Smith, 2007). To investigate the impact of baroclinic instability on eddy intensity at the seasonal scale, EOF analysis on the EGR of upper ocean

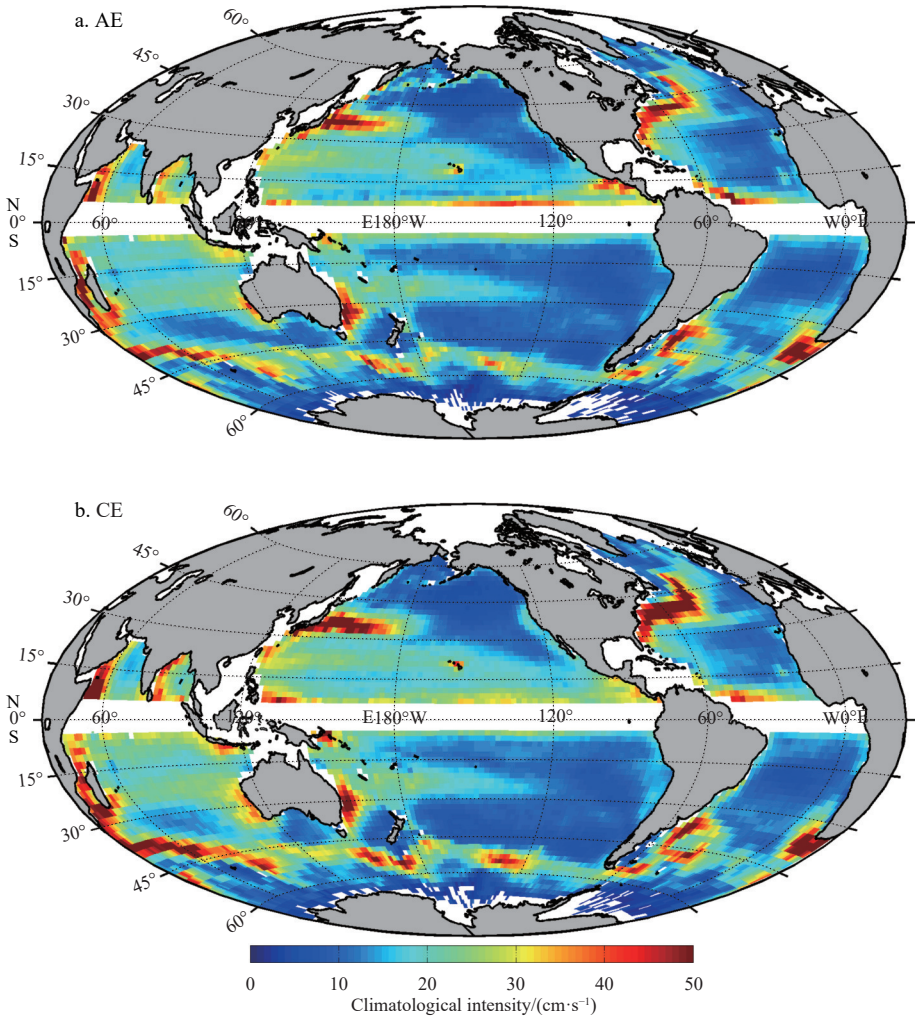

Fig. 3.

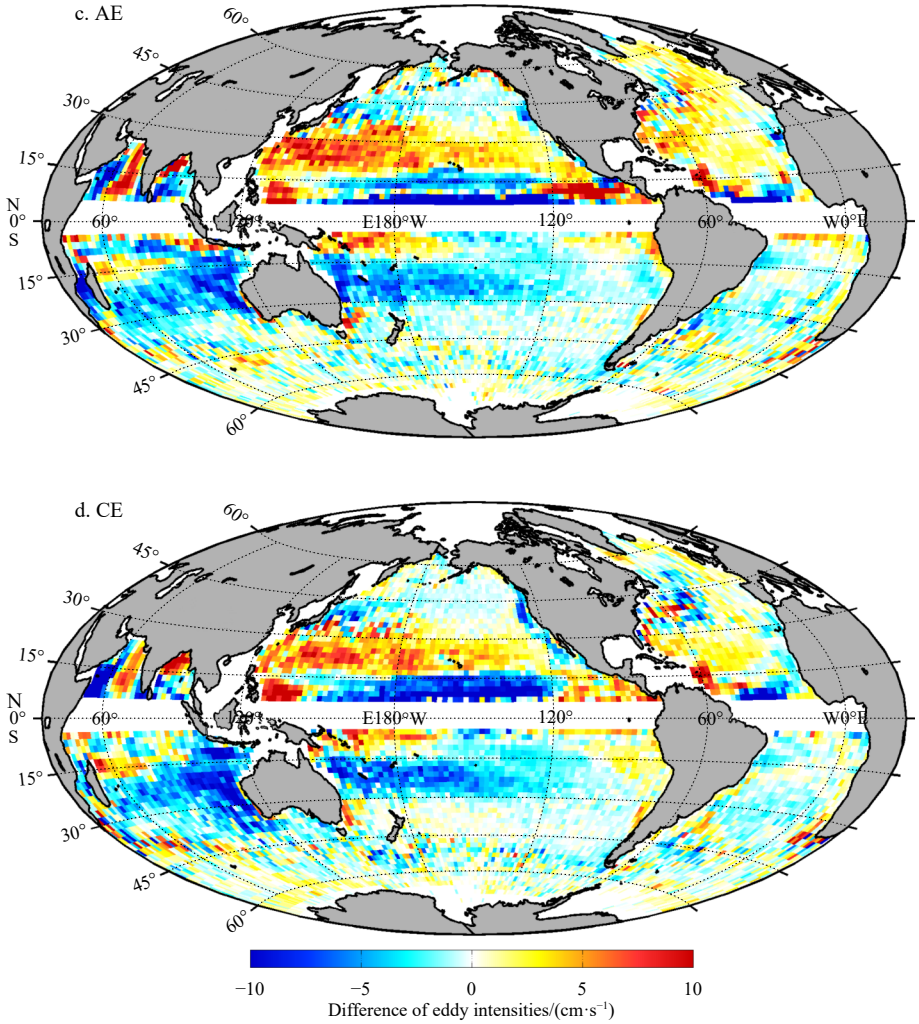

Fig. 3. Climatological intensity (cm/s) of AEs (a) and CEs (b) averaged from all months in 1993–2021. c and d. The seasonal differences between AEs and CEs, which are calculated by the mean difference of eddy intensities (cm/s) between winter and summer.

layers averaged from the surface to 200 m depth is conducted, and its first mode is displayed in Fig. 4. The spatial pattern of EOF1 of EGR (Fig. 4a) is highly consistent with that of eddy intensity. The temporal pattern of EOF1 in Fig. 4b indicates that EGR has obvious seasonal variation, consistent with previous studies (Qiu, 1999; Zhai et al., 2008). Different from the seasonal variation of eddy intensity, however, EGR reaches a peak in boreal winter while attaining a minimum in boreal summer (Fig. 4c). The spatial pattern of EOF1 is also verified by the maximum difference distribution (Fig. S4) of EGR between winter and summer.

After filtering, EOF1 of the original data mainly represents the seasonal signals. Compared to other modes, EOF1s of eddy intensity and EGR are both significant at the 95% confidence level tested by the Monte Carlo method (Livezey and Chen, 1983). In addition, when EOF is applied to a regional field, the variance contribution rate of EOF1 is significantly increased, and the spatiotemporal characteristics of the modes are unchanged (figures not shown). This indicates that EOF applied on a global scale does not lose the seasonal signals of the main mode.

To further verify the results of EOF and analyze the relationship between eddy intensity and EGR, the original time series averaged from four regions (Fig. 2a) with strong seasonality in the northwestern Pacific Ocean, the northwestern Atlantic Ocean, the eastern Indian Ocean, and the southwestern Pacific Ocean are selected. The monthly time series (Fig. S5) of eddy intensity and EGR reveal obvious seasonal cycles and a lead-lag relationship between eddy intensity and EGR. The mean annual cycles in Fig. 5 further distinctly display the prominent seasonal variations of eddy intensity and EGR. The peaks of eddy intensity and EGR occur in the spring and winter in the Northern Hemisphere, respectively. For the maximum values of eddy intensity and EGR in the Southern Hemisphere, the corresponding seasons turn to autumn and summer, respectively. The seasonal cycle amplitude (the difference between the maximum and minimum of 12 monthly averages of the mean annual cycle) reaches 5.2 cm/s, 2.4 cm/s, 5.0 cm/s, and 4.2 cm/s for eddy intensity in the northwestern Pacific Ocean, the northwestern Atlantic Ocean, the eastern Indian Ocean, and the Southwestern Pacific Ocean, representing ~23%, ~14%, ~23%, and ~25% of the mean values, respectively. For EGR, the seasonal cycle amplitude reaches 0.09 d^{-1}, 0.06 d^{-1}, 0.09 d^{-1}, and 0.08 d^{-1} in these four regions, representing ~78%, ~59%, ~56%, and ~67% of the mean values, respectively. The difference in the percentage between eddy intensity and EGR implies that the ratios of the energy converted to eddy through EGR are different between seasons in the annual cycle. Lagged cross-correlation analysis calculated from the monthly time series shown in Fig. S5 indicates that the seasonal variation of

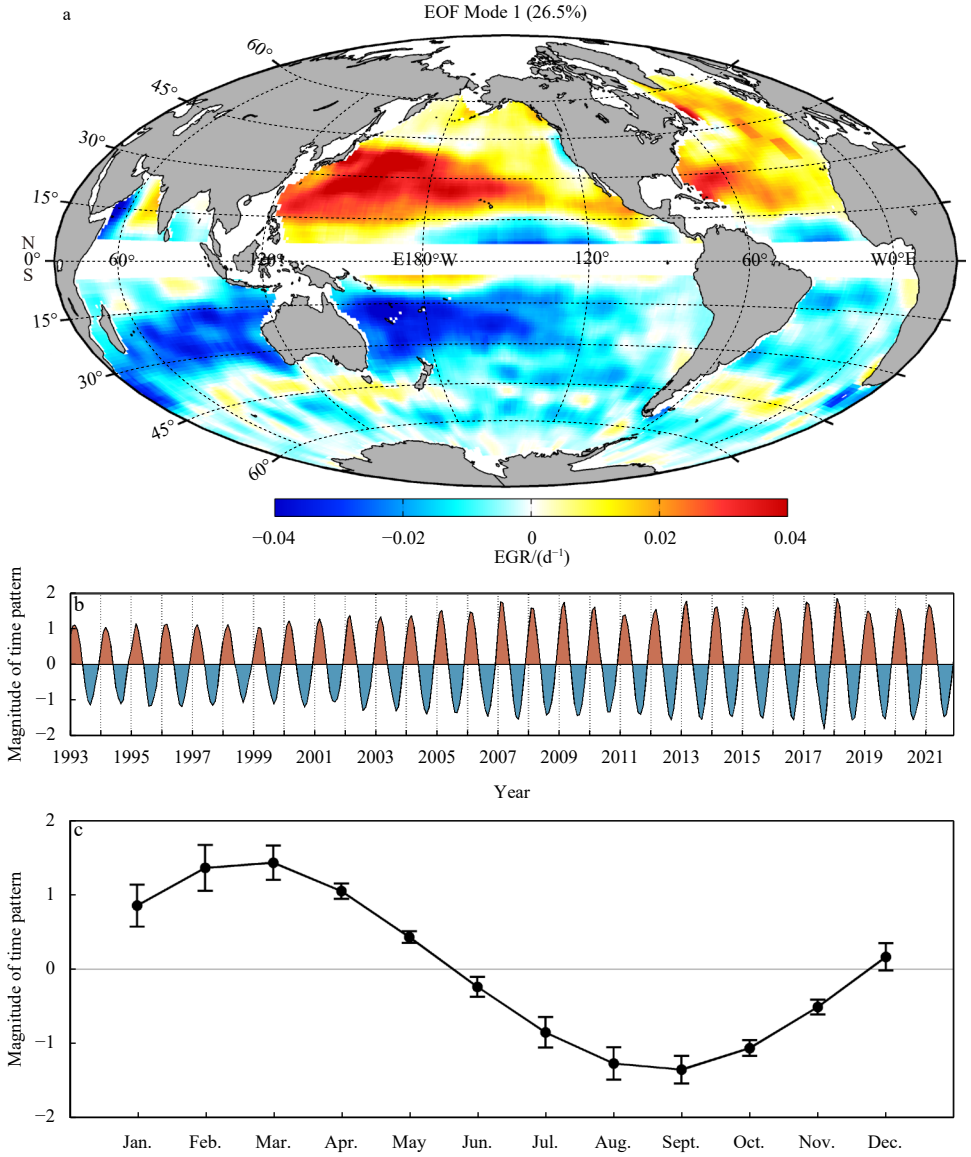

Fig. 4. First EOF mode of the EGR over the global ocean from January 1993 to December 2021: spatial pattern (a) and time pattern (b). The mode explains 26.5% of the eddy intensity variance. c. Times series of the monthly mean of the EOF1 time pattern. The error bars show the standard deviation (SD) of the EGR in the corresponding month.

eddy intensity lags behind that of EGR in phase by 2–3 months (Fig. 6). Specifically, in the northwestern Pacific Ocean, the northwestern Atlantic Ocean, and the southwestern Pacific Ocean, the correlation coefficients between eddy intensity and EGR reach the largest values which are 0.77, 0.68, and 0.84, respectively, when EGR takes lead by 3 months. In the eastern Indian Ocean, the maximum correlation coefficient (0.79) is achieved when the lead time turns to 2 months. A two-tailed Student's *t*-test estimated from the effective DOF (62, 85, 65, and 61 in the North Pacific Ocean, the North Atlantic Ocean, the South Indian Ocean and the South Pacific Ocean) calculated from the time series as described in the method section, suggests that all of the correlations are significant at the 95% confidence level.

4 Discussion

Barotropic instability is also an important mechanism for mesoscale eddy generation (Zu et al., 2022). To check the role of barotropic instability in the seasonal variation of eddy intensity, we calculated the BTR by using absolute geostrophic velocity. Figure 7 shows the seasonal difference of BTR and its smoothed field. It can be seen that BTR changes sharply in strong currents regions (such as the Kuroshio extension, the Gulf Stream region, the western Arabian Sea, the Antarctic Circumpolar Current areas in the Southern Ocean), and some offshore areas. However, in the regions with strong seasonal variation of eddy intensity, the seasonal changes of BTR are not significant, which is different from that in baroclinic instability (Fig. 3 or Fig. S4). This indicates that barotropic instability plays a less important role in seasonal variation of eddy intensity than baroclinic instability on a global scale.

Baroclinic instability develops in the flow where both rotation and stratification are important, as they are at the oceanic mesoscale and act to convert the mean available potential energy to EKE (Smith, 2007). At the seasonal scale, the EKE maximum lags behind the instability peak due to the approximately 2 months required for the initial perturbations of baroclinic in-

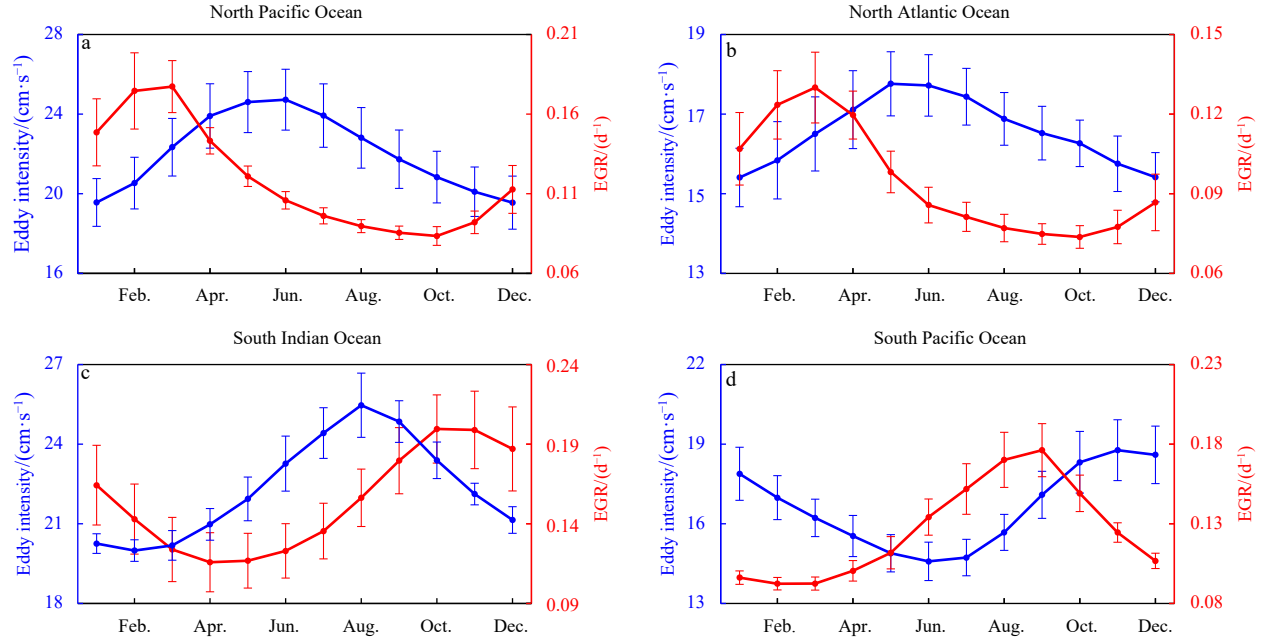

Fig. 5. Time series of the monthly mean eddy intensity (cm/s) and EGR (d^{-1}) averaged in the North Pacific Ocean (a. 15°N–30°N, 120°E–170°W), the North Atlantic Ocean (b. 15°N–30°N, 30°W–80°W), the South Indian Ocean (c. 15°S–30°S, 70°E–115°E) and the South Pacific Ocean (d. 15°S–30°S, 160°E–120°W), which are indicated with thick solid rectangular boxes in Fig. 2a.

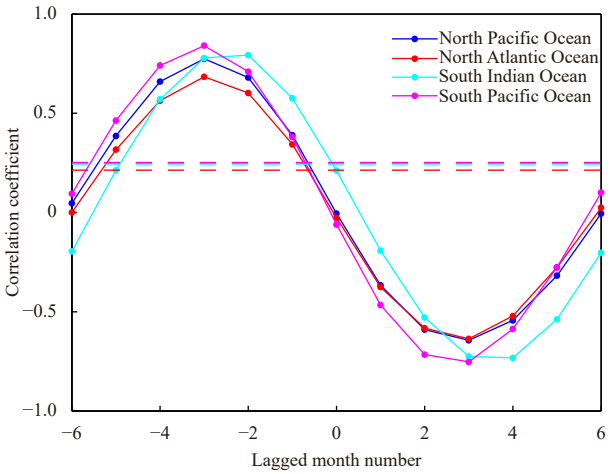

Fig. 6. Lagged correlation between the time series (shown in Fig. S5) of eddy intensity (cm/s) and EGR (d^{-1}). The critical values estimated from DOF (62, 85, 65, and 61 in the North Pacific Ocean, the North Atlantic Ocean, the South Indian Ocean and the South Pacific Ocean) at the 95% confidence level by the two-tailed Student's *t*-test are approximately 0.25, 0.21, 0.24, and 0.25, respectively, which are indicated by the corresponding dash lines. A positive lag indicates that eddy intensity takes the lead.

stability to grow into finite amplitude eddies under geostrophic turbulence (Qiu et al., 2014; Chang and Oey, 2014). This is also the reason why the eddy intensity needs 2–3 months to reach the maximum after the instability peak. N^2 represents the vertical gradient of water density, while vertical shear represents the horizontal gradient of water density derived from the thermal wind relation. Both of them together control the three-dimensional motions of water particles and then affect changes in baroclinic instability. The stratification has a vertical damping effect, and its seasonality in the upper layer affects the intensity of the surface signal of eddies (Bashmachnikov and Carton, 2012; Bashmachnikov et al., 2014). Qiu (1999) reported that the seasonal variation of baroclinic instability is subject to background stratification, which is strongly influenced by local heating/cooling in the North Pacific Subtropical region. For mesoscale eddies, regardless of cyclonic or anticyclonic type, their dynamic structures are the same in the open oceans. The most critical part is the horizontal geostrophic flow, which induces the vertical movement of water in the eddy center under the action of divergence or convergence. The vertical movement of water is the necessary condition for eddy generation, i.e., eddies are not easy to generate or develop when their vertical motions are suppressed. Meanwhile, the vertical shear of currents provides the energy source for the baroclinic instability to persist throughout the year (Stammer, 1997; Qiu, 1999; Qiu et al., 2014) and tends to force the generation of eddies (Zhang et al., 2020).

The spatial differences in eddy intensity are mainly caused by the change in EGR, which may be attributed to the meridional gradients of the upper oceanic stratification and the zonal gradients of vertical shear. In the meridional direction, the uneven distribution of heat caused by the solar shortwave radiation leads to the meridional gradients of the upper oceanic stratification, while the zonal gradients of vertical shear are due to the current fields with different intensity between eastern and western basins in the zonal direction. Although stratification and vertical shear together affect the generation and development of eddies, their contributions to the seasonal variation of baroclinic instability on the global scale still need to be further analyzed with high-resolution models in future research.

In addition, different from the seasonal variations, the trends of seasonal eddy intensity increase significantly in the strong currents regions (such as Kuroshio extension, Gulf Stream region, and Southern Ocean (Antarctic Circumpolar Current areas)) in the last three decades (Fig. S6), which may relate to the acceleration of upper ocean currents under global warming (Hu et al., 2020; Peng et al., 2022; Shi et al., 2023).

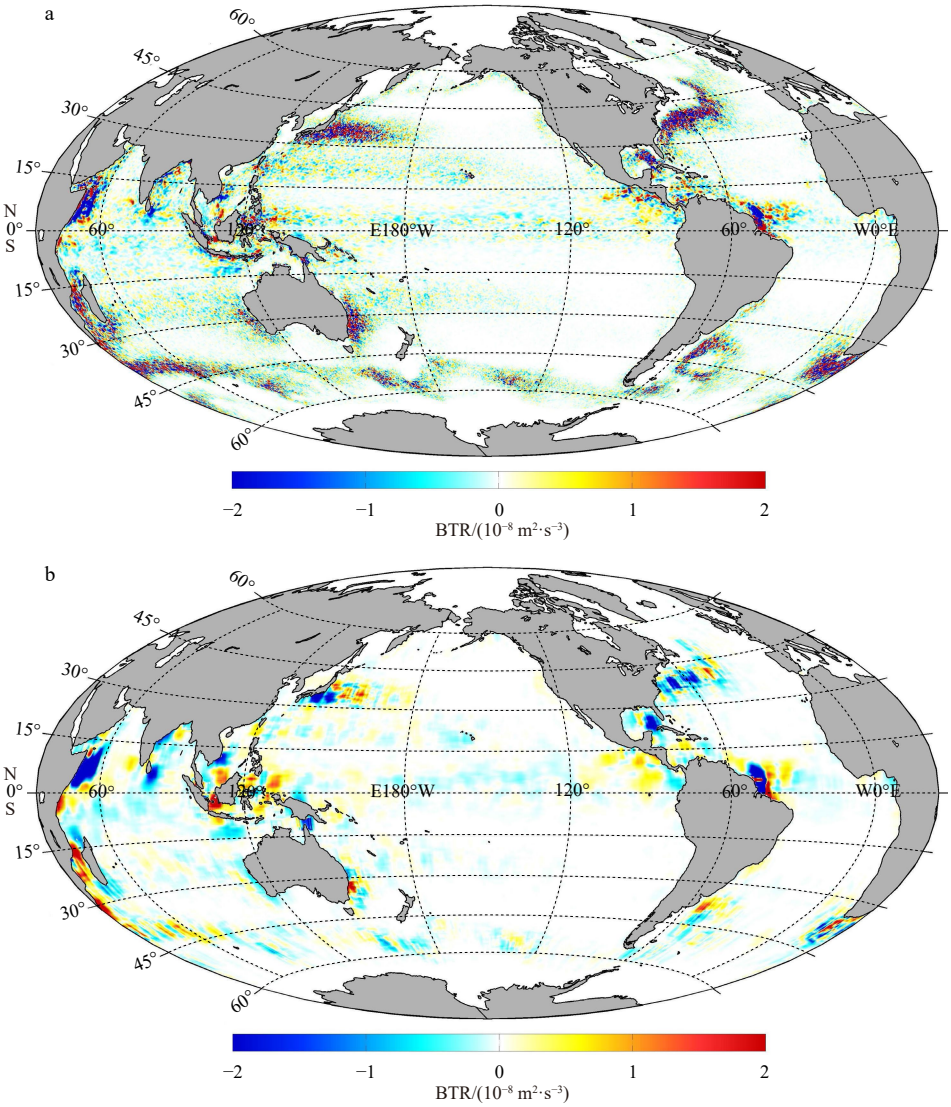

Fig. 7. The seasonal difference distribution of BTR (10^{-8} m^2/s^3) between winter and summer was calculated from the raw data set (a) and corresponding spatial smoothed field (b) with 2° × 2° smoothing length.

5 Summary

Using the latest satellite-altimetry-derived eddy trajectory data set, we documented the seasonal spatiotemporal variations of mesoscale eddy intensity in the global ocean. The results show that it has remarkable seasonal variations, reaching a peak in spring while attaining a minimum in autumn in the Northern Hemisphere and the opposite in the Southern Hemisphere. The conspicuous areas are primarily located in the tropical-subtropical transition zones within latitudinal bands between 15° and 30° in the main open oceans, except for 20°S to 35°S in the Southern Atlantic Ocean. In the tropical-subtropical transition zones of the western Pacific Ocean, the northwestern Atlantic Ocean, and the eastern Indian Ocean, the eddy intensity shows the strongest seasonal variations.

The seasonality in EGR is mainly responsible for the seasonal variations of eddy intensity. The spatial pattern of seasonal variation in EGR is highly consistent with that in eddy intensity. However, there is a lead-lag relationship between the temporal series of both. In the western Pacific Ocean and the northwestern Atlantic Ocean, the seasonal variation of eddy intensity lags behind that of EGR in phase by 3 months, while it turns to 2 months in the eastern Indian Ocean. The delay of the eddy intensity maximum in spring behind the instability peak in winter is due to the time (2–3 months) required for the initial perturbations of baroclinic instability to grow into finite amplitude eddies.

Acknowledgements

The altimetric Mesoscale Eddy Trajectory Atlas product (META3.2 DT allsat, doi: 10.24400/527896/a01-2022.005.220209) was produced by SSALTO/DUACS and distributed by AVISO+ with support from CNES, in collaboration with IMEDEA. The detailed link to the data information and access is as follows: https://www.aviso.altimetry.fr/en/data/products/value-added-products/global-mesoscale-eddy-trajectory-product/meta3-2-dt.html. The EN4.2.2 dataset is from Met Office Hadley Centre, which is open-access on the website: https://www.metoffice.gov.uk/hadobs/en4/download-en4-2-2.html. The absolute geostrophic current (doi: 10.48670/moi-00148) is published by Copernicus Marine Service and the access address is https://data.marine.copernicus.eu/product/SEALEV EL_GLO_PHY_L4_MY_008_047/services.

References

Aguedjou H M A, Dadou I, Chaigneau A, et al. 2019. Eddies in the tropical Atlantic Ocean and their seasonal variability. Geophysical Research Letters, 46(21): 12156–12164, doi: 10.1029/2019GL083925

Andersson M, Orvik K A, Lacasce J H, et al. 2011. Variability of the Norwegian Atlantic Current and associated eddy field from surface drifters. Journal of Geophysical Research: Oceans, 116(C8): C08032, doi: 10.1029/2011JC007078

Bashmachnikov I, Carton X. 2012. Surface signature of Mediterranean water eddies in the Northeastern Atlantic: Effect of the upper ocean stratification. Ocean Science, 8(6): 931–943, doi: 10.5194/os-8-931-2012

Bashmachnikov I, Carton X, Belonenko T V. 2014. Characteristics of surface signatures of Mediterranean water eddies. Journal of Geophysical Research: Oceans, 119(10): 7245–7266, doi: 10.1002/2014JC010244

Böning C W, Budich R G. 1992. Eddy dynamics in a primitive equation model: Sensitivity to horizontal resolution and friction. Journal of Physical Oceanography, 22(4): 361–381, doi: 10.1175/1520-0485(1992)022<0361:EDIAPE>2.0.CO;2

Bretherton C S, Widmann M, Dymnikov V P, et al. 1999. The effective number of spatial degrees of freedom of a time-varying field. Journal of Climate, 12(7): 1990–2009, doi: 10.1175/1520-0442(1999)012<1990:TENOSD>2.0.CO;2

Chaigneau A, Eldin G, Dewitte B. 2009. Eddy activity in the four major upwelling systems from satellite altimetry (1992–2007). Progress in Oceanography, 83(1–4): 117–123, doi: 10.1016/j.pocean.2009.07.012

Chaigneau A, Gizolme A, Grados C. 2008. Mesoscale eddies off Peru in altimeter records: Identification algorithms and eddy spatio-temporal patterns. Progress in Oceanography, 79(2–4): 106–119, doi: 10.1016/j.pocean.2008.10.013

Chang Y L, Oey L Y. 2014. Instability of the North Pacific subtropical countercurrent. Journal of Physical Oceanography, 44(3): 818–833, doi: 10.1175/JPO-D-13-0162.1

Chelton D B, Gaube P, Schlax M G, et al. 2011a. The influence of nonlinear mesoscale eddies on near-surface oceanic chlorophyll. Science, 334(6054): 328–332, doi: 10.1126/science.1208897

Chelton D B, Schlax M G, Samelson R M. 2011b. Global observations of nonlinear mesoscale eddies. Progress in Oceanography, 91(2): 167–216, doi: 10.1016/j.pocean.2011.01.002

Chen Gengxin, Gan Jianping, Xie Qiang, et al. 2012. Eddy heat and salt transports in the South China Sea and their seasonal modulations. Journal of Geophysical Research: Oceans, 117(C5): C05021, doi: 10.1029/2011JC007724

Chen Gengxin, Wang Qiang, Chu Xiaoqing. 2021. Accelerated spread of Fukushima's waste water by ocean circulation. The Innovation, 2(2): 100119, doi: 10.1016/j.xinn.2021.100119

Chu Xiaoqing, Xue Huijie, Qi Yiquan, et al. 2014. An exceptional anticyclonic eddy in the South China Sea in 2010. Journal of Geophysical Research: Oceans, 119(2): 881–897, doi: 10.1002/2013JC009314

Dong Changming, McWilliams J C, Liu Yu, et al. 2014. Global heat and salt transports by eddy movement. Nature Communications, 5: 3294, doi: 10.1038/ncomms4294

Eady E T. 1949. Long waves and cyclone waves. Tellus, 1(3): 33–52, doi: 10.3402/tellusa.v1i3.8507

Faghmous J H, Frenger I, Yao Yuanshun, et al. 2015. A daily global mesoscale ocean eddy dataset from satellite altimetry. Scientific Data, 2: 150028, doi: 10.1038/sdata.2015.28

Frenger I, Gruber N, Knutti R, et al. 2013. Imprint of Southern Ocean eddies on winds, clouds and rainfall. Nature Geoscience, 6(8): 608–612, doi: 10.1038/ngeo1863

Frenger I, Münnich M, Gruber N, et al. 2015. Southern Ocean eddy phenomenology. Journal of Geophysical Research: Oceans, 120(11): 7413–7449, doi: 10.1002/2015JC011047

Frenger I, Münnich M, Gruber N. 2018. Imprint of Southern Ocean mesoscale eddies on chlorophyll. Biogeosciences, 15(15): 4781–4798, doi: 10.5194/bg-15-4781-2018

Gaube P, McGillicuddy D J, Chelton D B, et al. 2014. Regional variations in the influence of mesoscale eddies on near-surface chlorophyll. Journal of Geophysical Research: Oceans, 119(12): 8195–8220, doi: 10.1002/2014JC010111

Good S A, Martin M J, Rayner N A. 2013. EN4: Quality controlled ocean temperature and salinity profiles and monthly objective analyses with uncertainty estimates. Journal of Geophysical Research: Oceans, 118(12): 6704–6716, doi: 10.1002/2013JC009067

Halo I, Penven P, Backeberg B, et al. 2014. Mesoscale eddy variability in the southern extension of the East Madagascar Current: Seasonal cycle, energy conversion terms, and eddy mean properties. Journal of Geophysical Research: Oceans, 119(10): 7324–7356, doi: 10.1002/2014JC009820

He Yinghui, Feng Ming, Xie Jieshuo, et al. 2017. Spatiotemporal variations of mesoscale eddies in the Sulu Sea. Journal of Geophysical Research: Oceans, 122(10): 7867–7879, doi: 10.1002/2017JC013153

Hu Shijian, Sprintall J, Guan Cong, et al. 2020. Deep-reaching acceleration of global mean ocean circulation over the past two decades. Science Advances, 6(6): eaax7727, doi: 10.1126/sciadv.aax7727

Kurczyn J A, Beier E, Lavín M F, et al. 2012. Mesoscale eddies in the northeastern Pacific tropical-subtropical transition zone: Statistical characterization from satellite altimetry. Journal of Geophysical Research: Oceans, 117(C10): C10021, doi: 10.1029/2012JC007970

Kurian J, Colas F, Capet X, et al. 2011. Eddy properties in the California Current System. Journal of Geophysical Research: Oceans, 116(C8): C08027, doi: 10.1029/2010JC006895

Liu Yu, Dong Changming, Guan Yuping, et al. 2012. Eddy analysis in the subtropical zonal band of the North Pacific Ocean. Deep-Sea Research Part I: Oceanographic Research Papers, 68: 54–67, doi: 10.1016/j.dsr.2012.06.001

Livezey R E, Chen W Y. 1983. Statistical field significance and its determination by Monte Carlo techniques. Monthly Weather Review, 111(1): 46–59, doi: 10.1175/1520-0493(1983)111<0046:SFSAID>2.0.CO;2

Martínez-Moreno J, Hogg A M, England M H. 2022. Climatology, seasonality, and trends of spatially coherent ocean eddies. Journal of Geophysical Research: Oceans, 127(7): e2021JC017453, doi: 10.1029/2021JC017453

Mason E, Pascual A, McWilliams J C. 2014. A new sea surface height-based code for oceanic mesoscale eddy tracking. Journal of Atmospheric and Oceanic Technology, 31(5): 1181–1188, doi: 10.1175/JTECH-D-14-00019.1

Pegliasco C, Busché C, Faugère Y. 2022. Mesoscale eddy trajectory atlas PRODUCT META3.2 DT. https://doi.org/10.24400/527896/A01-2022.005.220209[2022-09-27/2023-06-01]

Peng Qihua, Xie Shangping, Wang Dongxiao, et al. 2022. Surface warming-induced global acceleration of upper ocean currents. Science Advances, 8(16): eabj8394, doi: 10.1126/sciadv.abj8394

Qiu Bo. 1999. Seasonal eddy field modulation of the North Pacific Subtropical Countercurrent: TOPEX/Poseidon observations and theory. Journal of Physical Oceanography, 29(10): 2471–2486, doi: 10.1175/1520-0485(1999)029<2471:SEFMOT>2.0.CO;2

Qiu Bo, Chen Shuiming. 2013. Concurrent decadal mesoscale eddy modulations in the Western North Pacific Subtropical Gyre. Journal of Physical Oceanography, 43(2): 344–358, doi: 10.1175/JPO-D-12-0133.1

Qiu Bo, Chen Shuiming, Klein P, et al. 2014. Seasonal mesoscale and submesoscale eddy variability along the North Pacific Subtropical Countercurrent. Journal of Physical Oceanography, 44(12): 3079–3098, doi: 10.1175/JPO-D-14-0071.1

Robinson A R, McWilliams J C. 1974. The baroclinic instability of the open ocean. Journal of Physical Oceanography, 4(3): 281–294, doi: 10.1175/1520-0485(1974)004<0281:TBIOTO>2.0.CO;2

Schütte F, Brandt P, Karstensen J. 2016. Occurrence and characteristics of mesoscale eddies in the tropical northeastern Atlantic Ocean. Ocean Science, 12(3): 663–685, doi: 10.5194/os-12-663-2016

Shi Fei, Luo Yiyong, Wu Renhao, et al. 2023. Contrasting trends in

short-lived and long-lived mesoscale eddies in the Southern Ocean since the 1990s. Environmental Research Letters, 18(3): 034042, doi: 10.1088/1748-9326/acbf6b

Shum C K, Werner R A, Sandwell D T, et al. 1990. Variations of global mesoscale eddy energy observed from Geosat. Journal of Geophysical Research: Oceans, 95(C10): 17865–17876, doi: 10.1029/JC095iC10p17865

Smith K S. 2007. The geography of linear baroclinic instability in Earth's oceans. Journal of Marine Research, 65(5): 655–683, doi: 10.1357/002224007783649484

Stammer D. 1997. Global characteristics of ocean variability estimated from regional TOPEX/POSEIDON altimeter measurements. Journal of Physical Oceanography, 27(8): 1743–1769, doi: 10.1175/1520-0485(1997)027<1743:GCOOVE>2.0.CO;2

Stammer D. 1998. On eddy characteristics, eddy transports, and mean flow properties. Journal of Physical Oceanography, 28(4): 727–739, doi: 10.1175/1520-0485(1998)028<0727:OECETA>2.0.CO;2

Sun Wenjin, Dong Changming, Wang Ruyun, et al. 2017. Vertical structure anomalies of oceanic eddies in the Kuroshio Extension region. Journal of Geophysical Research: Oceans, 122(2): 1476–1496, doi: 10.1002/2016JC012226

Sun Bowen, Liu Chuanyu, Wang Fan. 2019. Global meridional eddy heat transport inferred from Argo and altimetry observations. Scientific Reports, 9(1): 1345, doi: 10.1038/s41598-018-38069-2

Yang Guang, Yu Weidong, Yuan Yeli, et al. 2015. Characteristics, vertical structures, and heat/salt transports of mesoscale eddies in the southeastern tropical Indian Ocean. Journal of Geophysical Research: Oceans, 120(10): 6733–6750, doi: 10.1002/2015JC011130

Zhai Xiaoming, Greatbatch R J, Kohlmann J D. 2008. On the seasonal variability of eddy kinetic energy in the Gulf Stream region. Geophysical Research Letters, 35(24): L24609, doi: 10.1029/2008GL036412

Zhang Ningning, Liu Guoqing, Liu Qinyan, et al. 2020. Spatiotemporal variations of mesoscale eddies in the Southeast Indian Ocean. Journal of Geophysical Research: Oceans, 125(8): e2019JC015712, doi: 10.1029/2019JC015712

Zhang Zhiwei, Tian Jiwei, Qiu Bo, et al. 2016. Observed 3D structure, generation, and dissipation of oceanic mesoscale eddies in the South China Sea. Scientific Reports, 6: 24349, doi: 10.1038/srep24349

Zhang Zhengguang, Wang Wei, Qiu Bo. 2014. Oceanic mass transport by mesoscale eddies. Science, 345(6194): 322–324, doi: 10.1126/science.1252418

Zhou Kuanbo, Xu Yanping, Kao Shuh-Ji, et al. 2023. Changes in nutrient stoichiometry in responding to diatom growth in cyclonic eddies. Geoscience Letters, 10: 12, doi: 10.1186/s40562-023-00269-8

Zu Yongcan, Fang Yue, Sun Shuangwen, et al. 2022. The seasonality of mesoscale eddy intensity in the Southeastern Tropical Indian Ocean. Frontiers in Marine Science, 9: 855832, doi: 10.3389/fmars.2022.855832

Zu Yongcan, Sun Shuangwen, Zhao Wei, et al. 2019. Seasonal characteristics and formation mechanism of the thermohaline structure of mesoscale eddy in the South China Sea. Acta Oceanologica Sinica, 38(4): 29–38, doi: 10.1007/s13131-018-1222-4

Supplementary information:

Fig. S1. Climatological field of amplitude (cm, color) of mesoscale eddies overlapped with their propagation speeds (cm/s, arrow). The climatology was averaged from 1993 to 2021.

Fig. S2. Time series of the monthly mean eddy intensity (cm/s) averaged in the western Arabian Sea (a. 5°N–20°N, 50°E–65°E), the North Pacific Ocean (b. 5°N–15°N, 125°W–165°W), the Southern Ocean (c. 50°S–60°S, 30°E–110°E) and the South Pacific Ocean (d. 5°S–11°S, 165°E–160°W), which are indicated with thin dotted rectangular boxes in Fig. 2a.

Fig. S3. The mean difference distribution of eddy intensity (cm/s) between spring and autumn was calculated from the raw data set (a) and corresponding spatial smoothed field (b).

Fig. S4. The mean difference distribution of EGR (d^{-1}) between winter and summer was calculated from the raw data set (a) and corresponding spatial smoothed field (b).

Fig. S5. Monthly times series of eddy intensity (cm/s) and EGR (d^{-1}) averaged in the four regions which are same with those (a. the North Pacific Ocean; b. the North Atlantic Ocean; c. the South Indian Ocean; d. the South Pacific Ocean) in Fig. 5.

Fig. S6. Decade trends [(cm/s)/decade] of eddy intensity in spring (a) and autumn (c), and their corresponding smoothing fields (b and d).

The supplementary information is available online at https://doi.org/10.1007/s13131-023-2278-3. The supplementary information is published as submitted, without typesetting or editing. The responsibility for scientific accuracy and content remains entirely with the authors.